Journal of Magnetic Resonance Open 16-17 (2023) 100134

Contents lists available at ScienceDirect

Journal of Magnetic Resonance Open

journal homepage: www.sciencedirect.com/journal/journal-of-magnetic-resonance-open

Research article

A nitroxide-containing cathode material for organic radical batteries studied with pulsed EPR spectroscopy

Ilia Kulikov [a], Anatoliy A. Vereshchagin [a,b], Daniil A. Lukianov [b], Oleg V. Levin [b], Jan Behrends [a,*]

[a] Berlin Joint EPR Lab, Freie Universität Berlin, Fachbereich Physik, Arnimallee 14, D-14195, Berlin, Germany
[b] Electrochemistry Department, St. Petersburg State University, 7/9 Universitetskaya nab., 199034, St. Petersburg, Russian Federation

ARTICLE INFO

Keywords:
Pulsed EPR
Electrochemistry
ORB
Nitroxide
Relaxometry
Instantaneous diffusion

ABSTRACT

An electron spin echo in a nitroxide-containing polymer cathode film for organic radical batteries is observed for various states of charge at cryogenic temperatures. The EPR-detected state of charge (ESOC), as inferred from the number of paramagnetic centers in the film, is compared to the results of Coulomb counting based on galvanostatic charging. Spin concentration, longitudinal relaxation times T_1 and phase memory times T_m strongly correlate with the ESOC. In the discharged film, the spin concentration reaches $(5 \pm 3) \times 10^{20}$ cm^{-3}, causing a phase memory time $T_m \ll 100$ ns (shorter than the resonator ring-down time) that hinders the detection of the spin echo. In the charged film, the decreased spin concentration results in a longer T_m between 100 ns and 300 ns that enables spin-echo detection, yet limits the length of the microwave pulse sequence. The short, broad-band pulses cause instantaneous diffusion in the unoxidized domains across the oxidized film, affecting the relative peak intensities in the pulsed EPR spectrum. By simulating the spectral distortion caused by instantaneous diffusion, we obtain information on the local spin concentration, which complements the information on the 'bulk' spin concentration determined by electrochemistry and continuous-wave EPR spectroscopy.

1. Introduction

Stable, capacious and powerful electrochemical energy sources, or batteries, are of great demand for today's energy driven society [1–3]. The advances in lithium ion technology for rechargeable batteries have enabled energy densities that make it possible to battery-power a wearable Internet-of-things device [4,5], an airplane [6] or a house [7,8]. Still, the application of lithium ion batteries is limited by irreversible processes [9–11] that occur upon extreme operating conditions such as high power demand [12,13] or over-discharge [14]. Such degradation processes limit the performance of a battery by lowering its safe operating power, resulting in lower power density and longer charging times. The challenge to overcome these limitations, together with low abundance of the rare earth metals [2] and the toxicity of the manufacturing process [15,16], is motivating research and development of advanced battery technologies [17]. This requires understanding of charge transport and degradation pathways in energy storage materials as well as exploring novel materials such as materials based on organic precursors [18,19].

Organic radical batteries (ORB) based on redox polymers containing stable radicals [20] have been shown to compete with or even outperform conventional Li based batteries in terms of power densities [21] with the additional benefit of being free from rare precursors, inheriting mechanical properties of plastics and electrical properties of semiconductors [22–24]. Advanced molecular design techniques allow for tuning of the electrochemical properties of the redox polymers [25], that brings in a rich variety of organic energy storage materials [25–27] and creates a large room for their optimization.

Redox conductive conjugated polymers containing TEMPO (2,2,6,6-tetramethylpiperidine-1-oxyl) redox groups, as pDiTBuS (poly-di-TEMPO-Butyl-Salen) shown in Fig. 1, demonstrate particularly promising energy and power densities [28]. The pDiTBuS was designed as a cathode material: it is oxidized when the electrochemical cell containing this material is charged. A film of pDiTBuS comprises a high concentration of redox active stable nitroxyl radicals attached to a conjugated polymer backbone that interconnects them as a molecular wire. Such system can be viewed as a highly disordered molecular hole-transporting semiconductor (the poly-NiSalen backbone) that contains a large amount of hole traps (TEMPO groups) attached to it with butyl linkers. When the film is reduced (discharged), the TEMPO groups are in the radical state and act as unfilled traps. Upon oxidation (charging), the TEMPO fragments lose an unpaired electron and acquire a positive

* Corresponding author.
E-mail address: j.behrends@fu-berlin.de (J. Behrends).

https://doi.org/10.1016/j.jmro.2023.100134
Received 25 June 2023; Received in revised form 25 September 2023; Accepted 29 September 2023
Available online 13 October 2023

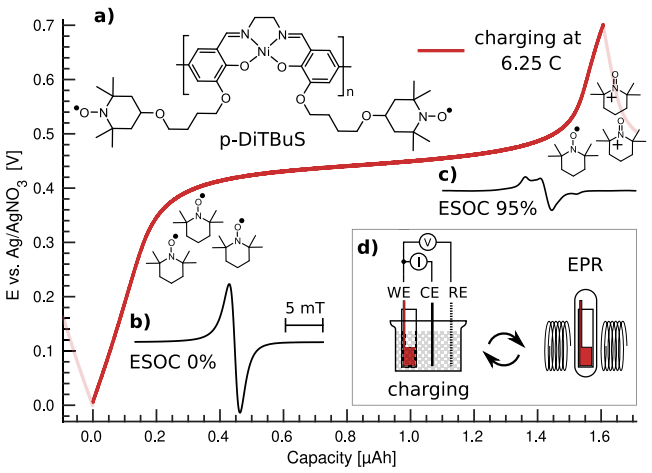

Fig. 1. Galvanostatic charge–discharge curve for a pDiTBuS cathode film at 10 μA (6.25 C), chemical structure of pDiTBuS (a), normalized cwEPR spectral signatures for reduced (b) and oxidized (c) states. Scheme of the ex-situ EPR measurement on the pDiTBuS half cell (d).

charge, so the traps are being filled with holes. The reversible redox reaction in the pDiTBuS film is demonstrated in a cyclic voltammogram shown in Figure S1 (see ESI).

The flexible molecular design together with questions regarding unresolved charge-transport and performance limiting mechanisms have inspired a variety of characterization techniques to be developed and applied to both energy storage materials and energy storage devices, operando and ex-situ. Together with electrochemical characterization as the standard method for studying the properties of energy storage materials [21,29], operando optical microscopy [30], neutron imaging [14] and X-ray diffraction [31] were applied to monitor irreversible structural deformations during extreme charging of Li cells.

UV and IR spectroscopy turned out to be particularly useful for studying organic energy-storage materials. For instance, it was possible to observe formation of positive polarons in the NiSalen backbone of the pDiTBuS upon its oxidation [32]. Since the electrochemical processes happen within the bulk of the energy storage material and involve changes in the spin states, imaging techniques based on magnetic resonance can be applied to obtain structural information on the battery electrodes on the molecular level [33–36]. NMR was used to study dendrite formation, electrolyte dynamics and intercalation of Li ions [37,38] in Li cells, including operando imaging [39]. Operando continuous-wave EPR (cwEPR) was applied to study redox kinetics of inorganic battery cathodes [40], radical formation and spin densities in redox polymers [32] and in organic electrochemical cells [41,42].

Pulsed EPR (pEPR) provides an even more powerful toolbox for material studies with the electron spin as a microscopic structural probe. In particular, pEPR provides access to the dipolar coupling between neighboring electron spins and thus the possibility to determine distances between adjacent redox-active centers using dipolar spectroscopy [43] as in spin-labeled proteins [44,45]. In addition, the hyperfine coupling between electron and nuclear spins in close vicinity can be measured by electron spin echo envelope modulation (ESEEM) and electron nuclear double resonance (ENDOR) techniques and can thus elucidate the degree of delocalization for charge carriers in ORB materials in a similar way as in organic semiconductors [46].

However, the high spin concentration in energy storage materials at certain states of charge (SoC) implies strong inter-spin interactions that lead to decoherences between the excited spins, so the spin echo in such densely packed spin systems usually decays much quicker than in the well studied dilute systems such as proteins [44] or intrinsic organic semiconductors [47]. The quick spin echo decay limits the maximum length of the microwave pulse sequence and raises a challenge [48] to apply the pEPR techniques to energy storage materials. In spite of these limitations, pEPR was used for estimating inter-spin distances in a polymer energy storage material ex situ [49] and for identifying the side reactions in the electrolyte of a Li cell upon degradation [50]. Very recently [51], pEPR was used to probe the electrical contact between TEMPO and activated carbon in a TEMPO-containing composite electrode material [21] made of non-conductive PTMA (poly(2,2,6,6-tetramethylpiperidinyloxy-4-yl methacrylate)) mixed with the conductive carbon additive. The efficiency of the TEMPO/carbon contact was determined by carefully analyzing the distributions of the spin-lattice relaxation times T_1. The phase memory time T_m in an array of closely spaced spins depends on the inter-spin distance [52]. T_m values, therefore, critically depend on the local spin concentration.

Here we report cwEPR and pEPR signals detected in a pDiTBuS polymer cathode film for various SoC that correspond to spin concentrations between 3.0×10^{19} cm^{-3} and 5.3×10^{20} cm^{-3}. At low SoC, the concentration of paramagnetic centers is high, the spin relaxation time is short and the spin echo cannot be detected. For higher SoC, the spin echo is detectable, yet the echo-detected field sweep (EDFS) spectrum shows relative peak intensities unusual for a nitroxide radical, as it is affected by instantaneous diffusion caused by strong inter-spin interactions. These results pave the way for studying the local molecular environment of electrochemically inactive sites in organic energy-storage materials using advanced pEPR techniques.

2. Materials and methods

2.1. Material

The material of interest is the redox-active polymer pDiTBuS (cf. Fig. 1a), i.e. a charge storage material that consists of TEMPO redox active molecular fragments [27,44,53] interconnected by a redox conductive conjugated NiSalen backbone [28,32]. DiTBuS was synthesized in the Levin group at the Saint-Petersburg State University. PDiTBuS exhibits a specific capacity up to 75 mAh g^{-1} and high charging rates. The molecular structure of pDiTBuS is similar to the previously reported pDiTS [28,42], except for a higher electrochemical stability and a more efficient electro-polymerization, that allows for growing thicker films.

2.2. PDiTBuS electrochemical cell for ex situ EPR spectroscopy

PDiTBuS was grown as a thin film on an on-substrate flat 3×4 mm^2 Au working electrode (WE) of a three-electrode cell as depicted in Fig. 1d, by means of electrochemical polymerization. The on-substrate WE was a 180 nm layer of Au deposited on a 3.5 mm wide quartz substrate using metal evaporation through a shadow mask, with a 7 nm Cr adhesion layer. For the electrochemical polymerization, the electrochemical cell was filled with DiTBuS monomers dissolved in the electrolyte (0.1 M Acetonitrile solution of Tetraethylammonium Tetrafluoroborate), and the voltage between the WE and the Pt counter electrode (CE) was repeatedly cycled between −200 mV and 800 mV with respect to the calibrated, Ag/10 mM $AgNO_3$ (Acetonitrile) reference electrode (RE) at a rate of 50 mV s^{-1} (for the cyclic voltammograms recorded during electrodeposition see ESI, Figure S1). After 50 electropolymerization cycles the pDiTBuS film had a capacity of 1.6 μAh with an estimated mass of 20–30 μg and a thickness of 800–1000 nm (see ESI, Section S3.2 for calculations)

The pDiTBuS film was brought to a desired SoC with the electrochemical setup shown in Fig. 1d. The container was filled with pure electrolyte (without DiTBuS monomers) and a static current of ±10 μA was applied between WE and CE for changing the electric potential of the film. The potential of the film during charging and discharging was recorded with respect to the RE as the Galvanostatic Charge–Discharge (GCD) curve (Fig. 1 and Figure S3 in the ESI). When the GCD reached a desired potential, the WE was disconnected from the

Table 1
EPR-detected state of charge, Coulomb counting and the corresponding spin concentrations in a galvanostatically discharging pDiTBuS film with $I = -10$ μA. The electric potential of the film E was measured with respect to the $Ag/AgNO_3$ RE. The number of injected (negative) elementary charges and the corresponding concentration of charges n_C were determined from the drawn capacity. The average spin concentration $\langle n \rangle$ is the ratio between the number of spins measured with quantitative cwEPR and the volume of the film determined by integrating the cyclic voltammogram. C is the local spin concentration in the film estimated with pEPR as described in text.

E [mV]	SoC	ESOC	Capacity drawn [μAh]	Charges injected	Spins detected	n_C [cm^{-3}]	$\langle n \rangle$ [cm^{-3}]	C [cm^{-3}]
590 ± 5	98%	(95 ± 1)%	0.020 ± 0.005	$(5 \pm 1) \times 10^{14}$	$(4 \pm 1) \times 10^{14}$	$(3 \pm 2) \times 10^{19}$	$(3 \pm 2) \times 10^{19}$	$>1 \times 10^{19}$
500 ± 5	96%	(85 ± 2)%	0.060 ± 0.005	$(1.4 \pm 0.1) \times 10^{15}$	$(1.1 \pm 0.1) \times 10^{15}$	$(1.0 \pm 0.5) \times 10^{20}$	$(8 \pm 4) \times 10^{19}$	$>3 \times 10^{19}$
430 ± 5	65%	(49 ± 3)%	0.480 ± 0.005	$(1.07 \pm 0.01) \times 10^{16}$	$(3.5 \pm 0.2) \times 10^{15}$	$(8 \pm 4) \times 10^{20}$	$(3 \pm 2) \times 10^{20}$	–
-200 ± 5	0%	(0 ± 5)%	1.360 ± 0.005	$(3.05 \pm 0.01) \times 10^{16}$	$(6.9 \pm 0.4) \times 10^{15}$	$(2 \pm 1) \times 10^{21}$	$(5 \pm 3) \times 10^{20}$	–

current source and the substrate with the pDiTBuS film was removed from the cell. The substrate was dried in pre-vacuum and flame sealed in a 5 mm OD quartz tube under 500 mbar of He. The tube was then frozen in liquid N_2 (77 K) and transported to the pre-cooled EPR spectrometer. In order to alter the SoC of the film between the EPR measurements, the tube was gradually warmed up to room temperature and opened, then the substrate with the charged film was removed from the tube and placed to the electrochemical setup where it was fully charged from the preserved SoC to 700 mV and discharged to the next desired SoC galvanostatically (ESI, Figure S4). After charging, the substrate was dried and encapsulated as described. SoC corresponding to −200 mV, 430 mV, 500 mV and 590 mV vs. the RE were considered. The potentials correspond to 0%, 65%, 96% and 98% of the full 1.4 μAh discharging capacity of the film, determined with Coulomb counting [54]. The charging capacity of the film has decreased by 12% upon repeated charging and temperature cycling, cf. ESI, Figure S2 and Section S2.3.

2.3. EPR-detected state of charge (ESOC)

The SoC of the film determined with Coulomb counting were compared to quantitative cwEPR to directly relate the number of charges, injected into the film upon charging, to the number of paramagnetic centers in it. We refer to the fraction of spins removed from the fully discharged film to reach a given SoC as the EPR-detected state of charge, or ESOC. The fully discharged film has the maximum number of spins and its ESOC is 0%. ESOC at other SoC are determined as the fraction of the missing spins with respect to ESOC 0%. ESOC of 95% thus corresponds to the oxidation state where only 5% of the initially present spins are left in the film. The cwEPR spectra were recorded for the listed SoC, and the corresponding numbers of spins were calculated from the double integrals of the spectra. The integrated spectra and the experimental details are shown in the ESI, Section S3.2. The injected charges, detected spins and ESOC values are counted for each SoC in Table 1. The average spin concentration in the film $\langle n \rangle$ at each ESOC was calculated from the corresponding number of spins and the estimated volume of the film of $(1.3 \pm 0.6) \times 10^{-5}$ cm^3.

2.4. Experimental details

EPR measurements for each SoC were performed at X-band (9.6 GHz) using a Bruker Elexsys E 580 spectrometer equipped with a 1 kW TWT microwave amplifier and an ER 4118 X-MD5 dielectric ring resonator cooled with a controlled flow of liquid He. EPR spectra were recorded at 80 K using a 200 mW cw microwave source at various attenuations and 0.5 mT modulation of the magnetic field at 100 kHz. Pulsed EPR was measured at 80 K and at 5 K using a 2-pulse sequence $(\pi/2 - \tau - \pi - \tau - echo)$ with a 20 ns long $\pi/2$ pulse and 11 dB high power attenuation. Quantitative cwEPR measurements for determining ESOC 0% were carried out at 80 K. Further experimental details are given in the ESI, Section S1

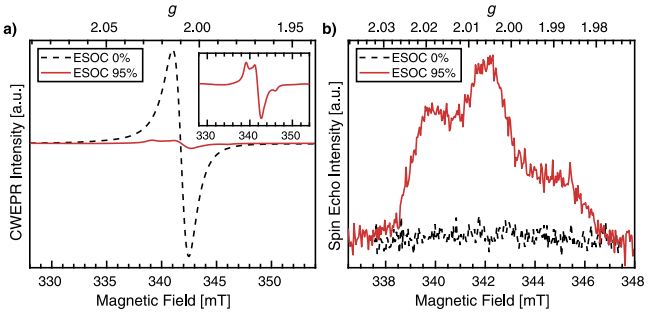

Fig. 2. (a): cwEPR spectra for reduced (fully discharged, ESOC 0%, dashed black) and oxidized (charged, ESOC 95%, solid red) pDiTBuS cathode film at 80 K. Inset: zoomed-in cwEPR spectrum for ESOC 95%. (b): EDFS spectra for the respective ESOC. (For interpretation of the references to color in this figure legend, the reader is referred to the web version of this article.)

3. Results and discussion

3.1. cwEPR vs. pEPR signals in pDiTBuS

A pDiTBuS film exhibits different cw and pulsed EPR signals depending on the ESOC. Fig. 2a shows cwEPR spectra of a pDiTBuS film in the charged (ESOC 95%) and in the discharged (ESOC 0%) states, measured at 80 K. The quantitative analysis of the cwEPR spectra reveals that the total number of spins and the average spin concentration in the film is decreasing from 5.3×10^{20} cm^{-3} (880 mM) at ESOC 0% down to 3.0×10^{19} cm^{-3} (50 mM), as listed in Table 1 and ESI, Section S3.2. The intermediate cwEPR spectra are shown in the ESI, Section S3.1. For the discharged state (ESOC 0%), due to the very high spin concentration, dipolar and exchange interactions broaden the cw line and average out the hyperfine components, leaving only a Lorentzian central line at $g = 2.007$ with a peak-to-peak width of 1.4 mT (black-dashed in Fig. 2a). While for high SoC the number of charges injected into the film (Table 1, "charges injected") is comparable to the number of spins detected with cwEPR ("spins detected"), there are only 22% of the injected charges that are detectable with cwEPR for low SoC. The discharge curve for low SoC ends after the plateau associated with the charging of TEMPO and implies the charging of the backbone (cf. Fig. 1, Figure S4 in the ESI). The fact that 78% of charges for SoC 0% are not detectable by EPR suggests that most of the charges injected into the film at low SoC 0% are in a diamagnetic ($S = 0$) EPR-silent state on the polymer backbone. The contribution of the backbone to the electrochemical capacity of pDiTBuS is less than 30%, so the diamagnetic states are formed both in the backbone and, possibly, also between neighboring TEMPO groups. We note that the significant discrepancy between n_C and $\langle n \rangle$ for 0% SoC was not observed in a previous study on a similar material (pDiTS) [42]. As the pDiTBuS film studied here was much thicker than the pDiTS film used in Ref. [42], we speculate that the film thickness has an influence on the formation of diamagnetic species and thus the difference between the number of charges determined by Coulomb counting and the number of paramagnetic centers extracted from quantitative EPR.

In contrast to the discharged film, the spectrum for the highly charged film (ESOC 95%, red-solid line in Fig. 2a) has a much lower

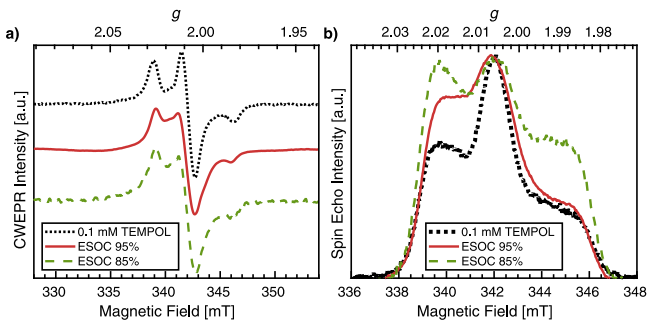

Fig. 3. (a): cwEPR spectra for pDiTBuS charged to 95% and 85%, and for a frozen 0.1 mM solution of TEMPOL. Normalized intensities. Temperature 80 K. (b): Corresponding pEPR spectra measured at 5 K. Intensities scaled by the $m_I = 0$ central peak.

cwEPR intensity that corresponds to a much lower number of spins (see Table 1, "spins detected"). With the decreased spin concentration at ESOC 95%, the exchange and dipolar interactions in the film become weaker and the hyperfine structure becomes resolved, leaving a typical signature of an isolated, immobilized nitroxide radical [55] that is also shown in the inset of Fig. 2a. Spectral simulations with the extracted hyperfine and g values are given in the ESI, Section S5. The EDFS signal for ESOC 95% is well detectable (Fig. 2b) and shows three peaks at the expected field positions for a nitroxide radical, albeit with a reduced intensity of the central peak as compared to a usual nitroxide spectrum [55] and to a 0.1 mM solution of non-interacting TEMPOL (4-hydroxy-2,2,6,6-tetramethylpiperidin-1-oxyl, Fig. 3b, dotted-black).

We now discuss the apparent suppression of the signal intensity for the central hyperfine component in the pEPR spectrum at 95% ESOC. This effect was previously observed in a similar, fully charged poly-di-TEMPO-Salen film and was attributed to isolated, electrochemically inactive domains [42] of paramagnetic nitroxide radicals. Therefore, the local spin concentration in the oxidized pDiTBuS film may be much higher than the average value (determined by quantitative cwEPR), which can induce instantaneous diffusion [43,45,52], as it was observed in highly concentrated solutions of SO_4^- radicals [43], in concentrated nitroxide spin labels [45] and in the PTMA/carbon mixture [51]. Instantaneous diffusion causes an additional anisotropic relaxation mechanism that distorts the relative spectral intensities in the echo-detected EPR spectra when short, broad-band microwave pulses are used to excite a densely packed spin system [43]. Instantaneous diffusion in a densely packed nitroxide system leads to the suppression of the central peak in the EDFS spectrum, as it was predicted [43] and observed [45,51]. Taking into account the similarity between the spectrum shown in Fig. 2b and the spectra presented in Ref. [51], we attribute the peculiar spectral shape observed for pDiTBuS to instantaneous diffusion.

While the spin echo is clearly detectable for the charged states, it cannot be detected in the discharged state. For the discharged state, the strong interspin coupling is causing a fast spin relaxation and a quick echo decay. The dead time of the spectrometer is t_d = 120 ns (Bruker Elexsys E 580 with overcoupled ER 4118 X-MD5 dielectric ring resonator, Q ≈ 300), so the detection of the spin echo is challenging in densely packed spin systems with $T_m \leq t_d$. The EDFS signals for pDiTBuS at ESOC ≤ 49% were indistinguishable from the resonator background even after an overnight scan at 5 K.

We now describe the influence of the ESOC on the pEPR spectra. The EDFS spectra of the charged film at ESOC 85% and ESOC 95% are shown in Fig. 3b. The spectra were recorded at 5 K to increase the signal intensity. The length of the $\pi/2$ pulse was 20 ns. The EDFS spectrum of a 0.1 mM solution of TEMPOL is shown in Fig. 3b (dotted-black) for comparison.

The EDFS spectrum for 85% ESOC (dashed-green in Fig. 3b) has a suppressed central peak when compared to a dilute solution of TEMPOL. The EDFS spectrum for 95% ESOC (solid-red in Fig. 3b) is closer to the TEMPOL spectrum than ESOC 85%, but has an increased intensity of the low-field peak. At the same time, the cwEPR spectral shapes are similar for ESOC 85%, ESOC 95% and TEMPOL, measured with similar parameters (Fig. 3a). The integrated cwEPR spectra have similar peak ratios (Figure S6 in the ESI). While the cwEPR spectra for pDiTBuS at high ESOC show a typical signature of isolated nitroxides (Fig. 3a), the corresponding pEPR spectra deviate from the nitroxide spectrum and strongly depend on the ESOC.

3.2. Instantaneous diffusion in charged pDiTBuS

We have seen that the ESOC has a strong influence on the shape of the EDFS spectra. Furthermore, the EDFS spectra of pDiTBuS are quite different from the reference spectrum of TEMPOL in a dilute frozen solution.

High spin concentration in a pDiTBuS electrode suggests strong inter-spin dipolar couplings which cause instantaneous diffusion when probed with short (broad-band) microwave pulses [45], as it was observed in a PTMA/carbon mixture [51]. Instantaneous diffusion caused by a broad-band microwave pulse shown in Fig. 4, dashed-red, manifests itself in an additional field-dependent spin relaxation factor $V(B_0)$, that alters the relative peak intensities in the echo-detected spectrum. For spins uniformly distributed in space, $V(B_0)$ is described [45] by Eq. (1):

$$V(B_0, 2\tau, C) = V_0(2\tau)\exp\left(-2\tau\frac{4\pi^2}{9\sqrt{3}}\gamma^2\hbar C\langle\sin^2(\theta/2)\rangle\right) \quad (1)$$

with

$$\langle\sin^2(\theta/2)\rangle = \frac{\int \frac{B_1^2}{(B-B_0)^2+B_1^2}\sin^2\left(\frac{\gamma t_p}{2}\sqrt{(B-B_0)^2+B_1^2}\right)g(B)\mathrm{d}B}{\int g(B)\mathrm{d}B} \quad (2)$$

where B_0 is the static magnetic field, C is the concentration of spins, τ is the time between the first and second pulses in the microwave pulse sequence, γ is the gyromagnetic ratio of the electrons at resonance, t_p is the duration of the second microwave pulse, B_1 is the amplitude of the second microwave pulse, $g(B)$ is the EDFS spectrum at $\tau = 0$ that is not affected by the instantaneous diffusion. As the resulting spectral shape depends on the spin concentration, comparing spectra simulated according to Eq. (1) and measured spectra thus allows us to provide information about the local spin concentrations. Since the spin echo of the most densely packed and thus quickly relaxing spins is not detectable with the given t_d, the regions of the highest spin concentration do not contribute to the EDFS spectrum. Thus, C is lower than the true concentration of spins in the densely packed domains and can also be lower than the average spin concentration $\langle n\rangle$ measured with cwEPR that is most sensitive to the quickly relaxing spins.

We have used a 50 mM solution of TEMPOL as a model system to explore how the excitation bandwidth affects instantaneous diffusion for nitroxides (see Section S7.1, ESI). The EDFS spectrum recorded with t_p = 40 ns and τ = 120 ns shows a distortion that corresponds to C = 9 mM, while for t_p = 1000 ns no effect of instantaneous diffusion is observed. We simulated the undistorted EDFS spectrum of TEMPOL using the Easyspin toolbox [56] for Matlab and obtained the g matrix and the hyperfine coupling tensor A (for simulation details see Section S6, ESI). Then we simulated the EDFS spectrum for pDiTBuS, ESOC 85%, using the obtained parameters and Eq. (1) with t_p = 40 ns and the concentration C as a fit parameter. The result of the simulation with $C = 3.1\times10^{19}$ cm^{-3} = 50 mM is shown in Fig. 4. At the same time, quantitative cwEPR yields a higher spin concentration for ESOC 85%: $\langle n\rangle = (8\pm4)\times10^{19}$ cm^{-3} = (130 ± 70) mM.

The ESOC 95% spectrum cannot be simulated with Eq. (1) because of the increased intensity of the low-field peak. The ratio of the two remaining peaks at ESOC 95% corresponds to $C = 1.2\times10^{19}$ cm^{-3} = 20 mM (see ESI, Section S7.4), while cwEPR again yields a higher $\langle n\rangle = (3\pm2)\times10^{19}$ cm^{-3} = (50 ± 30) mM .

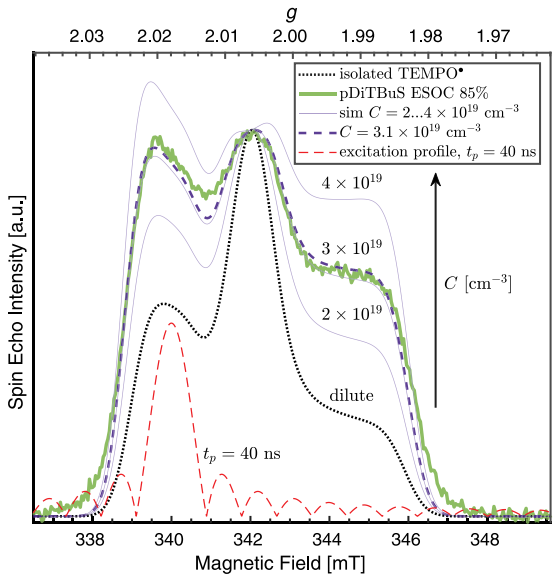

Fig. 4. EDFS spectrum of p-DiTBuS at ESOC 85% (solid-green) affected by instantaneous diffusion with t_p = 40 ns. Simulation of the spectrum with spin concentration $C = 3.1 \times 10^{19}$ cm^{-3} = 52 mM as a fit parameter (dashed-purple). Simulated spectrum of non-interacting TEMPO with g = [2.0099, 2.0055, 2.0026], A = [21.99, 21.43, 96.27] MHz and 0.812 mT (lwpp) Gaussian line shape as the starting values for the simulation (dashed-black). Excitation profile of the 40 ns pulse at B_0 = 340 mT is shown in dashed-red. (For interpretation of the references to color in this figure legend, the reader is referred to the web version of this article.)

3.3. Spin relaxation times in charged pDiTBuS

As we have shown in Section 3.2, the reason for the distorted spectral shape in pDiTBuS at ESOC 85% is instantaneous diffusion that manifests itself in anisotropic spin relaxation which alters the relative peak intensities. However, the spectrum for ESOC 95% cannot be simulated assuming just instantaneous diffusion (cf. Figure S27, ESI). In order to gain additional information about the processes that may influence the shape of the EDFS spectra, we performed field-dependent measurements of the spin relaxation times.

Fig. 5a shows the EDFS spectra of pDiTBuS for 85% and 95% ESOC as well as a reference sample (50 mM solution of TEMPOL in Dichloromethane:Acetonitrile (3:1) glass) measured at T = 5 K. The spectra reveal markedly different intensities of the three hyperfine components.

The changed relative peak intensities in pDiTBuS may be the result of a magnetic field-dependent spin relaxation mechanism that manifests itself in a field-dependent phase memory time T_m [52]. The T_m for pDiTBuS and for TEMPOL was probed in a field-swept echo decay experiment. The echo decay transients for the three samples are shown in Fig. 5b. A Hahn echo pulse sequence was used with a $\pi/2$ pulse length of 20 ns and variable pulse separation time $\tau \geq 120$ ns. Spin echo was detected at 2τ after the $\pi/2$ pulse. Periodic oscillations in the echo decay transients correspond to the ESEEM effect from protons [52] with $\Delta\omega_L \approx 15$ MHz, which are particularly pronounced for TEMPOL.

If the sample contains several different species (i.e. nitroxide radicals in different environments and/or different local concentration) with distinct spin–spin relaxation times, the echo decay transients may contain multiple decay components, so more than one T_m can correspond to each field point. This effect is not considered when simulating the effect of instantaneous diffusion using Eq. (1). To determine the number of decay components in the echo decay transients, we studied the poles of the Padé approximation of the Taylor expansion of the Laplace transforms of the transients that is known as the Padé-Laplace method [57] (see ESI, Section S4.1 for details). This analysis revealed only monoexponential spin echo decays for both 95% ESOC and 85% ESOC. We therefore assumed a monoexponential spin echo decay for pDiTBuS, though some faster relaxing components with $T_m < t_d$ might have decayed by the earliest achievable τ, as shown in Section S7.5, ESI. The detected decay times $T_m(B_0)$, extracted from fits of the background-corrected echo-decay curves, are shown in Fig. 5c as filled squares with the grayscale representing the amplitude of the corresponding fit component. As expected, T_m is significantly larger for 95% than for 85% ESOC, consistent with the weaker spin–spin couplings in the fully charged film. Further, we note that the field-dependence of T_m is more pronounced for 95% ESOC, with $T_m \geq 200$ ns for the $m_I = +1$ hyperfine component. This anisotropy in T_m results in an increased intensity of the low-field peak, which is in line with the observation that we cannot describe the 95% ESOC spectrum assuming only instantaneous diffusion (see Section 3.2). The transient fits and the residuals are shown in Section S4.1, ESI.

We attempted to reproduce the pDiTBuS spectra from a standard nitroxide spectrum by considering anisotropic transient decay of the spectral intensity at $t = \tau = 120$ ns for each B_0 with the measured $T_m(B_0)$. However, this approach did not allow us to reconstruct the pDiTBuS spectra for neither 85%, nor 95% ESOC.

It was recently shown that densely packed TEMPO radicals in a TEMPO-containing, non-conductive polymer PTMA, intermixed into an amorphous carbon mesh, show multiple spin-lattice relaxation times T_1 because of different types of contact between the TEMPO radicals and the conductive additive in the TEMPO/carbon composite [51]. In order to find out whether such behavior can also be observed for the porous pDiTBuS film, we measured spin-lattice relaxation times T_1 with an inversion-recovery pulse sequence ($p_I - \tau - \pi/2 - \tau_{fix} - \pi - \tau_{fix} - echo$) with p_I = 32 ns, $\frac{\pi}{2}$ = 20 ns and variable τ (Fig. 5d). The Padé-Laplace analysis yielded one decay component for TEMPOL and two decay components for pDiTBuS both at 85% ESOC and 95% ESOC (see ESI, Section S4.1.4 for details). The T_1 for charged pDiTBuS is on the same order as for TEMPOL and splits into two rather broad distributions with similar intensities (Fig. 5e). Similar as in the case of T_m, also T_1 is larger for 95% than for 85% ESOC. Irrespective of the ESOC there is no significant field dependence of T_1, in contrast to what is observed for the TEMPOL reference sample.

Daniel et al. [51] concluded that separate distributions of T_1 correspond to different binding between TEMPO and the carbon mesh, representing the quality of electrical contact between TEMPO and the conductive additive. With the observed distribution of T_1 and considering the two-component cwEPR spectral contributions for charged pDiTBuS (“broad” and “dilute” components, cf. Section S5, ESI), we suggest that two types of domains could exist in a partially charged pDiTBuS film as well. These two morphologies may correspond to “conductive” domains with shorter T_1, where TEMPO• are close to the conductive pNiSalen backbone, and “non-conductive” domains with longer T_1, where TEMPO• are separated from pNiSalen. We note, however, that based on the experimental data presented here, this interpretation is rather speculative. The detected T_1 values for pDiTBuS may also correspond to one distribution, as the separation between the T_1 values is comparable to the widths of their distributions.

3.4. Temperature dependence of pulse spectra of charged pDiTBuS

Spin relaxation times usually depend on temperature [52]. We measured EDFS of charged pDiTBuS at 5 K and at 80 K to see how faster spin relaxation affects the spectral shape. Fig. 6 shows EDFS spectra for pDiTBuS charged to ESOC 95% (a) and to ESOC 85% (b) at 80 K (solid) and at 5 K (dashed). At 80 K an overnight scan was required to obtain a satisfactory signal-to-noise ratio, whereas at 5 K the spectrum was recorded in a few minutes. The spectral intensities at different temperatures were scaled such that the high-field $m_I = -1$ peak has the same intensity. Fig. 6 clearly shows that the relative intensities of the peaks change with temperature for both ESOC. At higher temperatures the EDFS spectrum of pDiTBuS has a peak ratio closer to that of dilute

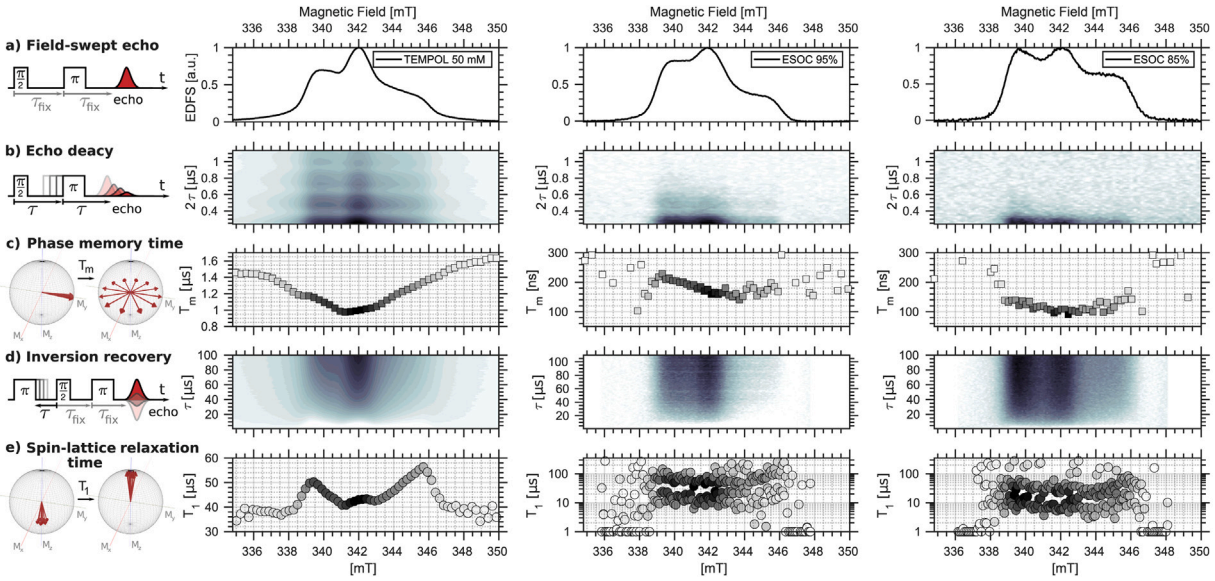

Fig. 5. Field-swept echo (a), echo decay transients (b), phase memory times T_m (c), inversion recovery (d) and spin-lattice relaxation times T_1 (e) measured in 50 mM frozen electrolyte solution of TEMPOL (left) and in dry pDiTBuS film charged to ESOC 95% (center) and to ESOC 85% (right). Temperature 5 K. Grayscale represents the intensity in (b)–(e).

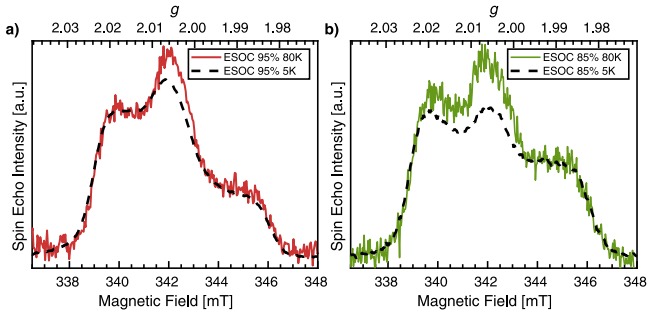

Fig. 6. EDFS spectra for pDiTBuS charged to 95% ESOC (a) and to 85% ESOC (b) measured at 5 K and at 80 K.

TEMPOL that corresponds to a lower spin concentration, according to Eq. (1). The influence of the temperature increase on the spectral shape is stronger for 85% ESOC.

The overall relaxation times in the film decrease with increasing temperature, but the dead time of the spectrometer (t_d = 120 ns) does not change. Therefore, at a given temperature, only spins with $T_m > t_d$ contribute to the signal. At higher temperature only the weakly coupled spins (with the longest T_m) are detectable, which results in a spectral shape that is less affected by instantaneous diffusion and thus closer to a dilute nitroxide solution.

4. Conclusion and perspectives

We connected the Coulomb-counting state of charge of a pDiTBuS film to the number of reduced and thus paramagnetic TEMPO moieties by measuring the number of spins at various SoC with cwEPR. The spin counting performed with cwEPR allowed us to determine the average spin concentration in a film at a given ESOC. The average spin concentration in the film changes upon oxidation between $(5\pm3)\times10^{20}$ and $(3\pm2)\times10^{19}$ cm^{-3}. At high SoC, the number of injected charges fits well to the number of EPR-detected charges. However, the lower the SoC, the larger fraction of the injected charges becomes EPR silent. At SoC 0%, the fraction of EPR silent charges is 78%. The concentration of injected charges at SoC 0% corresponds to the average distance between the charges of d = 0.8 nm, which may allow for a formation of singlet spin states (with $S = 0$) [58]. While all ESOC yield a measurable cwEPR signal, at ESOC ≤ 49% no spin echo can be observed.

The strong inter-spin interactions in the discharged battery cathode drastically reduce the phase memory time T_m of the spin packets probed by pEPR, especially for the domains with the highest concentration of spins. For ESOC < (49 ± 3)% with the average spin concentration $\langle n\rangle > (3\pm2)\times10^{20}$ cm^{-3}, the T_m becomes shorter than the spectrometer dead time t_d = 120 ns, thus by the time of detection, the spin echo becomes indistinguishable from the noise. The low values of T_m represent a challenge to measure pEPR in materials with $\langle n\rangle > 10^{20}$ cm^{-3}. The alternative, dead-time-free detection schemes [59–62] may be employed to overcome the limitation imposed by short T_m in energy storage materials. With the dead-time-free detection, the echo decay transients can be measured at earlier times $\tau < t_d$, allowing for detecting the spin echoes from the domains with higher spin concentrations. That would extend the range of the observable local spin concentration C and allow for precise identification of the charged domains in a battery electrode.

Spin-lattice relaxation times T_1, measured in the inversion recovery experiments, have revealed two types of domains in a partially charged pDiTBuS film. Both domain types may have comparable spin concentrations and therefore similar T_m. The "conductive" domains with shorter T_1 are likely to have a more efficient charge transfer kinetics between the TEMPO and the conductive pNiSalen backbone of pDiTBuS, while the "non-conductive" domains with longer T_1 have a weaker interaction between TEMPO and the environment, which implies a lower probability for electron transfer between the TEMPO and the backbone. However, the separation between the two T_1 distributions is rather small and the existence of the two domain types is debatable. The information extracted from the inversion recovery measurements can be used to differentiate between the domains of various charge transport efficiency, which can be used for optimizing the electrode material, such that one predominant type of domains is growing during electropolymerization.

The ability to detect a spin echo signal in a material with densely packed spins, as pDiTBuS, opens the intriguing perspective to apply advanced pulsed pEPR techniques to study novel battery materials on a molecular level. For instance, charge delocalization and intermolecular interactions in organic semiconductors can be observed with pEPR methods, particularly including double resonance techniques [47]. ENDOR was used for measuring charge delocalization in molecular semiconductor dopants [63]; electron–electron double resonance (ELDOR)

was used to measure interspin distances between spin-labeled sites in a protein [44] and to observe transient radical formation in photosystems [36]. The presented analysis of the instantaneous diffusion caused by the short microwave pulses and substantial inter-spin interactions provides information on the local spin concentrations in the cathode at various states of charge. Combined, the cwEPR, electrochemical and pEPR data help one to elucidate the charging of the battery electrode on a microscopic level, allowing for a detailed monitoring of the processes that lead to degradation of the electrode capacity, such as the formation of electrically disconnected domains (“dead mass”), and to improve the film deposition procedure by monitoring its morphology through the T_1 values.

Declaration of competing interest

The authors declare that they have no known competing financial interests or personal relationships that could have appeared to influence the work reported in this paper.

Data availability

Data will be made available on request.

Acknowledgments

This work was supported by the joint RSF-DFG grant program (RSF grant number 22-43-04414, DFG grant number BE 5126/7–1). We thank Naitik Panjwani, Robert Bittl, Christian Teutloff and Daria Dymnikova for insightful discussions.

Appendix A. Supplementary data

Supplementary material related to this article can be found online at https://doi.org/10.1016/j.jmro.2023.100134.

References

[1] H.D. Yoo, E. Markevich, G. Salitra, D. Sharon, D. Aurbach, Mater. Today 17 (2014) 110–121.
[2] C. Xu, Q. Dai, L. Gaines, M. Hu, A. Tukker, B. Steubing, Commun. Mater. 1 (2020) 1–10.
[3] N. Nitta, F. Wu, J.T. Lee, G. Yushin, Mater. Today 18 (2015) 252–264.
[4] Y.H. Lee, J.S. Kim, J. Noh, I. Lee, H.J. Kim, S. Choi, J. Seo, S. Jeon, T.S. Kim, J.Y. Lee, J.W. Choi, Nano Lett. 13 (2013) 5753–5761.
[5] P.K.R. Maddikunta, G. Srivastava, T.R. Gadekallu, N. Deepa, P. Boopathy, IET Intell. Transp. Syst. 14 (2020) 1388–1395.
[6] J. Kadlec, R. Cipin, D. Cervinka, P. Vorel, B. Klima, J. Solid State Electrochem. 18 (2014) 2307–2313.
[7] B. Diouf, C. Avis, J. Energy Storage 22 (2019) 295–301.
[8] T. Hirasawa, M. Yoshida, S. Obara, Int. J. Energy Res. 45 (2021) 807–823.
[9] F. Larsson, P. Andersson, P. Blomqvist, B.E. Mellander, Sci. Rep. 7 (2017) 1–13.
[10] Y. Fu, S. Lu, K. Li, C. Liu, X. Cheng, H. Zhang, J. Power Sources 273 (2015) 216–222.
[11] Q. Zhang, T. Liu, Q. Wang, J. Energy Storage 42 (2021) 1–9.
[12] G. Zhang, X. Wei, S. Chen, G. Han, J. Zhu, H. Dai, ACS Appl. Energy Mater. 5 (2022) 6462–6471.
[13] T. Guan, S. Sun, F. Yu, Y. Gao, P. Fan, P. Zuo, C. Du, G. Yin, Electrochim. Acta 279 (2018) 204–212.
[14] T. Ma, S. Wu, F. Wang, J. Lacap, C. Lin, S. Liu, M. Wei, W. Hao, Y. Wang, J.W. Park, ACS Appl. Mater. Interfaces 12 (2020) 56086–56094.
[15] A. Pražanová, V. Knap, D.I. Stroe, Energies 15 (2022) 1–29.
[16] J.F. Peters, M. Baumann, B. Zimmermann, J. Braun, M. Weil, Renew. Sustain. Energy Rev. 67 (2017) 491–506.
[17] F. Degen, M. Schütte, J. Clean. Prod. 330 (2022) 129798.
[18] Y. Lu, J. Chen, Nat. Rev. Chem. 4 (2020) 127–142.
[19] J. Kim, Y. Kim, J. Yoo, G. Kwon, Y. Ko, K. Kang, Nat. Rev. Mater. 8 (2023) 54–70.
[20] K. Nakahara, S. Iwasa, M. Satoh, Y. Morioka, J. Iriyama, M. Suguro, E. Hasegawa, Chem. Phys. Lett. 359 (2002) 351–354.
[21] H. Takeo Nishide, Suga, J. Soc. Mech. Eng. 110 (2007) 194–195.
[22] C. Friebe, U.S. Schubert, Top. Curr. Chem. 375 (2017) 1–35.
[23] N. Casado, D. Mecerreyes, RSC Polym. Chem. Ser. (2021) 1–26.
[24] N. Goujon, N. Casado, N. Patil, R. Marcilla, D. Mecerreyes, Prog. Polym. Sci. 122 (2021) 101449.
[25] T. Janoschka, C. Friebe, M.D. Hager, N. Martin, U.S. Schubert, ChemistryOpen 6 (2017) 216–220.
[26] Y. Xie, K. Zhang, Y. Yamauchi, K. Oyaizu, Z. Jia, Mater. Horiz. 8 (2021) 803–829.
[27] A.A. Vereshchagin, A.Y. Kalnin, A.I. Volkov, D.A. Lukyanov, O.V. Levin, Energies 15 (2022) 1–50.
[28] A.A. Vereshchagin, D.A. Lukyanov, I.R. Kulikov, N.A. Panjwani, E.A. Alekseeva, J. Behrends, O.V. Levin, Batter. Supercaps 4 (2020) 336–346.
[29] C. Zens, C. Friebe, U.S. Schubert, M. Richter, S. Kupfer, ChemSusChem e202201679 (2022) 1–14.
[30] A.J. Merryweather, Q. Jacquet, S.P. Emge, C. Schnedermann, A. Rao, C.P. Grey, Nature Mater. 21 (2022) 1306–1313.
[31] K.J. Rhodes, R. Meisner, M. Kirkham, N. Dudney, C. Daniel, J. Electrochem. Soc. 159 (2012) A294–A299.
[32] E. Dmitrieva, M. Rosenkranz, J.S. Danilova, E.A. Smirnova, M.P. Karushev, I.A. Chepurnaya, A.M. Timonov, Electrochim. Acta 283 (2018) 1742–1752.
[33] A. Niemöller, P. Jakes, S. Eurich, A. Paulus, H. Kungl, R.A. Eichel, J. Granwehr, J. Chem. Phys. 148 (2018) 1–10.
[34] C. Meier, J. Behrends, C. Teutloff, O. Astakhov, A. Schnegg, K. Lips, R. Bittl, J. Magn. Reson. 234 (2013) 1–9.
[35] C. Li, M. Shen, B. Hu, Wuli Huaxue Xuebao/ Acta Phys. - Chim. Sin. 36 (2019) 1–16.
[36] R. Bittl, S. Weber, Biochim. Biophys. Acta - Bioenergetics 1707 (2005) 117–126.
[37] T. Kushida, J.C. Murphy, Phys. Rev. B 21 (1980) 4247–4250.
[38] C. Grosu, C. Panosetti, S. Merz, P. Jakes, S. Seidlmayer, S. Matera, R. a Eichel, J. Granwehr, C. Scheurer, PRX Energy 2 (2023) 1–14.
[39] Y. Shi, M. Tang, Wuli Huaxue Xuebao/ Acta Phys. - Chim. Sin. 36 (2019) 1–13.
[40] A. Niemöller, P. Jakes, R.A. Eichel, J. Granwehr, Chem. Phys. Lett. 716 (2019) 231–236.
[41] Q. Huang, E.D. Walter, L. Cosimbescu, D. Choi, J.P. Lemmon, J. Power Sources 306 (2016) 812–816.
[42] I. Kulikov, N.A. Panjwani, A.A. Vereshchagin, D. Spallek, D.A. Lukianov, E.V. Alekseeva, O.V. Levin, J. Behrends, Energy Environ. Sci. 15 (2022) 3275–3290.
[43] K.M. Salikhov, S.A. Dzuba, A.M. Raitsimring, J. Magn. Reson. 42 (1981) 255–276.
[44] G. Jeschke, Annu. Rev. Phys. Chem. 63 (2012) 419–446, Vol. 63.
[45] Y.V. Toropov, S.A. Dzuba, Y.D. Tsvetkov, V. Monaco, F. Formaggio, M. Crisma, C. Toniolo, J. Raap, Appl. Magn. Reson. 15 (1998) 237–246.
[46] M. Fehr, J. Behrends, S. Haas, B. Rech, K. Lips, A. Schnegg, Phys. Rev. B 84 (2011) 1–5.
[47] C.E. Tait, A. Reckwitz, M. Arvind, D. Neher, R. Bittl, J. Behrends, Phys. Chem. Chem. Phys. 23 (2021) 13827–13841.
[48] M.K. Bowman, A.G. Maryasov, Appl. Magn. Reson. 52 (2021) 1041–1062.
[49] L. Assumma, Y. Kervella, J.M. Mouesca, M. Mendez, V. Maurel, L. Dubois, T. Gutel, S. Sadki, ChemSusChem 13 (2020) 2419–2427.
[50] C. Szczuka, P. Jakes, R.-A. Eichel, J. Granwehr, Adv. Energy Sustain. Res. 2 (2021) 1–10.
[51] D.T. Daniel, C. Szczuka, P. Jakes, R.-A. Eichel, J. Granwehr, Phys. Chem. Chem. Phys. 25 (2023) 12767–12776.
[52] A. Schweiger, G. Jeschke, Principles of Pulse Electron Paramagnetic Resonance, Oxford University Press, 2001, p. 247.
[53] K. Halbmair, J. Seikowski, I. Tkach, C. Höbartner, D. Sezer, M. Bennati, Chem. Sci. 7 (2016) 3172–3180.
[54] K. Movassagh, A. Raihan, B. Balasingam, K. Pattipati, Energies 14 (2021) 1–33.
[55] E. Bordignon, eMagRes 6 (2017) 235–254.
[56] S. Stoll, A. Schweiger, J. Magn. Reson. 178 (2006) 42–55.
[57] E.H. Hellen, Amer. J. Phys. 73 (2005) 871–875.
[58] J. Behrends, A. Schnegg, K. Lips, E.A. Thomsen, A.K. Pandey, I.D. Samuel, D.J. Keeble, Phys. Rev. Lett. 105 (2010) 1–4.
[59] A. Schweiger, R.R. Ernst, J. Magn. Reson. 77 (1988) 512–523.
[60] J. Granwehr, J. Forrer, A. Schweiger, J. Magn. Reson. 151 (2001) 78–84.
[61] E.A. Nasibulov, J. Behrends, L.V. Kulik, K.L. Ivanov, Z. Phys. Chem. 231 (2017) 269–291.
[62] F. Kraffert, D. Bahro, C. Meier, M. Denne, A. Colsmann, J. Behrends, J. Magn. Reson. 282 (2017) 10–17.
[63] M. Arvind, C. Tait, M. Guerrini, J. Krumland, A.M. Valencia, C. Cocchi, A.E. Mansour, N. Koch, S. Barlow, S.R. Marder, J. Behrends, D. Neher, J. Phys. Chem. B 124 (2020) 7694–7708.